Characterization of mesoscale geometrical features of a preform using spectral Moiré analysis on pressure print

S. Bancora, C. Binetruy, S. Advani, Sebastien Comas-Cardona

Version of Record: https://www.sciencedirect.com/science/article/pii/S1359835X21003225
Manuscript_248a7a9371bc6cf58582b887a3a5726e

Characterization of mesoscale geometrical features of a preform using spectral Moiré analysis on pressure print

S. Bancora[a,*], C. Binetruy[a,b], S. Advani[b,a], S. Comas-Cardona[a]

[a] *École Centrale de Nantes, Research Institute in Civil Engineering and Mechanics (GeM), UMR CNRS 6183, 44321 Nantes Cedex 3, France*
[b] *Center for Composite Materials, University of Delaware, Newark, Delaware 19716, USA*

Abstract

In the frame of LCM processes, the mesoscopic architecture of a preform is defined by the sequential stacking of layers in the mold. Once the compaction is carried out, the precise orientation of layers and spatial distribution of tows is difficult to know with precision. The lack of this information can lead to a wrong prediction of properties. In this work, we present a new non-destructive methodology to obtain information about the mesoscale architecture of a multi-layer preform in its compacted state. Using a flexible pressure-sensitive film, the compaction pressure field is captured. Data is analyzed using spectral Moiré theory to retrieve the orientation and spatial distribution of tows for each layer in the stack. This technique is non-destructive and scalable in size, making it suitable to characterize large preforms before infusion. The methodology is detailed and tested over a varying number of layers and configurations.

Keywords: Liquid composite moulding, Lay-up (manual/automated), Process monitoring, Spectral Moiré analysis

1. Introduction

During the manufacturing of composite parts using Liquid Composite Molding (LCM) processes, a stack of textile layers is compacted inside a mold and then im-

*Corresponding author
Email address: simone.bancora@ec-nantes.fr (S. Bancora)

pregnated with a liquid resin. Several variations exist, the differentiating factor usually being the type of mold used. The main two categories are represented by RTM, in which a two part rigid mould is used, and VARTM, where the upper mold is replaced by a flexible bag held under vacuum pressure [1]. Independent of the technique used, injection parameters must be tuned according to the characteristics of the part to ensure that all voids are filled by the resin [2, 3, 4]. Being able to predict the resin flow becomes important to reduce defects and consequently manufacturing costs. While the numerical modeling of the resin filling process is fairly advanced, the predicted flow patterns are a strong function of the preform permeability, which represents the mesoscale architecture of the compacted preform. Estimating the permeability of a given preform requires the knowledge of the orientation and arrangement of tows in the layers [5]. However, this information is not easy to obtain. Both the stacking and compaction stages have an influence on the spatial distribution of tows and orientation of the layers inside the closed mold, affecting the local permeability [6]. Furthermore fibrous textiles are characterized by a high degree of variability that cannot be taken into account a priori [7].

To overcome these uncertainties in the recent years we have witnessed a rising interest in characterization techniques based on the use of digital materials. These methods rely on creating a numerical twin of the material which is built at the scale of the tows (mesoscale) and resembles as closely as possible its physical counterpart. Besides the characterization of flow properties, digital materials can be used also to estimate the mechanical properties of the part or to simulate an entire manufacturing chain. In order to recreate realistic digital representations of a multi-layer preform, one needs to have access to three pieces of information about the tows: cross section geometry, orientation and spatial distribution. As a consequence there is a need for techniques of measurement and quantification of these features, and these measurements

must be carried out on the preform in its compacted, ready to be impregnated state.

Visual techniques were proposed to reconstruct the geometry of a textile [8, 9], with the limitation that this approach is only able to study the surface of a preform. A similar result was obtained from the study of a textile pressure signature [10], still limiting the technique to a single layer. Micro-tomography (μ-CT) allows to obtain very detailed measurements of the mesoscale geometry of the sample but the scalability of the technique is limited [11], making it unsuitable for large parts application. Thus, there are lack of techniques that allow one to measure the mesoscale features of a multi-layer preform in its compacted state over a large domain.

In the present work we propose such a technique which analyzes the pressure field experienced by a dry preform during compaction and measures the orientation and tow spatial frequency of every layer in the stack. This technique also allows to detect misalignment defects in periodic layups. The pressure exerted on the mold by the layers is captured using a non-intrusive pressure sensitive film that can be placed inside any rigid mold without any size limitations. The morphological similarity between UD textiles and gratings is exploited to apply the principles of Moiré theory to the patterns observed on the pressure field. Image spectral analysis is used to extract information from the pressure patterns. The information obtained can be used for the generation of realistic digital models of the preforms at the mesoscale, which can serve as input data for further characterization. The process is non-destructive, and can be integrated in current manufacturing workflow to provide characterization of the dry compacted preform before it is impregnated with resin. The methodology is demonstrated with example studies.

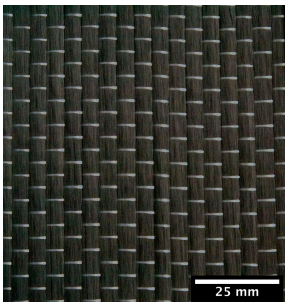

(a) Top view

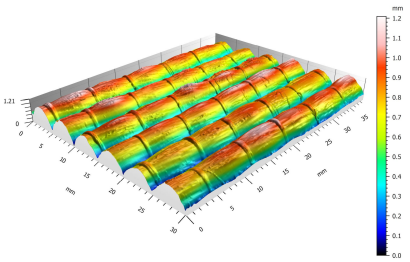

(b) 3D scan of the textile surface

Figure 1: C-Weave UT710P textile

2. Materials

The textile used in this study is a quasi-UD carbon fiber textile (C-Weave UT710P 50K T13 from Chomarat). This fabric is shown in Fig.1a. The 3D surface measurement of one layer of uncompressed textile was acquired using a confocal microscope to provide an accurate dimensional reference (Fig.1b). Average measurements are obtained for tow thickness: $h_{\text{meas}} = 1.3$ mm, tow width: $w_{\text{meas}} = 4.80$ mm and tow center-lines period: $T_{\text{meas}} = 5.12$ mm. The geometry of the warp yarn, which is one order of magnitude smaller than the carbon tows, is neglected in the rest of this study.

The measurement of the pressure exerted on the layers during compaction is carried out using a Prescale pressure system produced by Fujifilm. This sensor has been traditionally used for biomechanical applications [12] and more recently also with composites [10]. The sensor consists of a thin pressure-sensitive film, around 180 μm thick , that can be placed over a mold surface, and displays shades of color to quantify the pressure field from the contact force it senses when a specimen is pressed against it. One key advantage of Prescale over other electrical systems [13, 14] is that it can be laid over large mould surfaces in order to study full scale parts. The film can bend, however cannot be sheared. Therefore its application is limited to flat or single-curvature surfaces. A double-curvature mould pressure field could still be mapped by applying a patchwork of smaller films. Flexible sensors actually exist that overcome this limitation [15, 16],

but their cost and sensitivity range place them outside of the scope of this research. A calibration procedure for Prescale films can be found in [17]. Several gradations of films are available that address various ranges of pressure. In this work the LLLW version is used which can quantify the pressure between 0.2 and 0.6 MPa.

3. Methodology

This paper will illustrate how Moiré theory and spectral analysis can provide information about the structure of multiple fabric layers by examining its compaction pressure field imprinted on the Prescale film. Moiré patterns can be observed when two or more periodic structures are superimposed. A geometrical treatment of the patterns that are generated from superposition of periodic gratings can be found in [18]. Fourier theory of spectral analysis can be used to characterize Moiré structures. In the frequency domain, spatial patterns are easy to interpret as they can be decomposed into a series of cosinusoidal functions. An extensive treatment of the topic can be found in [19]. Theoretical material on the subject can also be found in [20, 21]. A brief overview of the theory and notation used is provided in Appendix A.

In the present work we take advantage of the similarity between layers of quasi-UD textile and periodic gratings. The underlying assumption is that the local thickness of one layer of textile roughly resembles a two-dimensional cosinusoidal field (grating) of the form:

$$r(x, y) = \frac{h}{2} \left(\cos[2\pi f(x \cos\theta + y \sin\theta)] + 1\right) \tag{1}$$

where h is the maximum tow thickness, θ is the orientation of the grating and f is its spatial frequency ($f = T^{-1}$ where T is the tow center-lines period). When multiple layers of textile are stacked and compressed, Moiré patterns appear due to the interaction between overlapping tows. The effect arises because of the waviness of

layer surfaces. The technique cannot provide information for perfectly flat textiles (the latter are rarely encountered for composite materials) . To investigate this behavior a series of tests were carried out. Multiple stacked plies of textile were compressed using an Instron 8805 hydraulic press, as to replicate the compaction phase in preform manufacturing. One Prescale LLLW film was placed under the preform to capture the pressure field exerted on the bottom plate. Since the range of pressure sensitivity of the film is limited, for all tests in this work the compression is driven by imposing an appropriate force equal to 30 kN. The compression is carried out at a very low speed of 0.5 mm/min to reduce viscoelastic effects. Force/displacement data is recorded, from which the final thickness of the compressed preform can be obtained. The Prescale film thickness is taken into account and subtracted from the measured value. Initial thickness (h_0, measured at 0.1 kN force) and final thickness (h_f, measured at 30 kN force) of all specimens are provided in Table 1.

For each test presented, the compression is carried out over a 30×30 cm plate and textile samples are 47×47 cm in size. This results in a nominal pressure of 0.33 MPa applied. The Prescale film used to capture the pressure field is placed at the center of this area and has dimensions of 21×27 cm. Each pressure-marked film is scanned and digitized using an Epson Workforce DS-5500 unit. To obtain consistent measurements, exposure and acquisition resolution (600 PPI) are manually set. The methodology is first illustrated for a layup of two angled plies, then extended to more layers. A complete list of all test cases is provided in Table 1.

3.1. Two Ply Stack

Two layers of textile were stacked on top of each other at different orientations. The first layer (bottom) was laid down along an orientation which is assumed as reference (0°). The second layer was placed on top of the first one at some angle θ_2 intentionally not measured, in order to create an unbiased generic layup. Care was taken to ensure

Table 1: List of test cases

Test case	Label	Number of plies	Sequence	h_0 [mm]	h_f [mm]
Two Ply Stack	2PS	2	$[0°, \theta_2]$	2.47	1.74
Four Ply Stack	4PS	4	$[0°, \theta_2, \theta_3, \theta_4]$	4.27	2.67
Four Ply Periodic (misaligned)	4PPm	4	$[0°, \theta_2] \times 2$	3.90	2.65
Four Ply Periodic (aligned)	4PPa	4	$[0°, \theta_2] \times 2$	3.87	2.59
Nine Ply Periodic (misaligned)	9PPm	9	$[0°, \theta_2, \theta_3] \times 3$	7.88	4.43
Nine Ply Periodic (aligned)	9PPa	9	$[0°, \theta_2, \theta_3] \times 3$	7.51	4.45

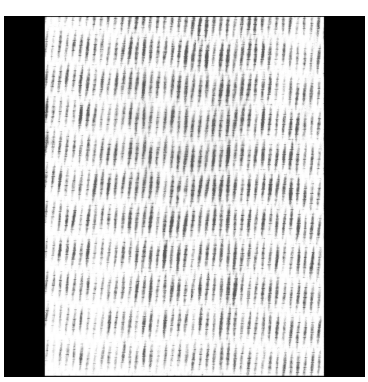

(a) Pressure field at 30 kN force

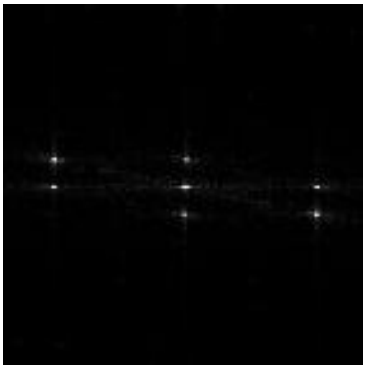

(b) $F(u, v)$ spectrum data (enhanced contrast)

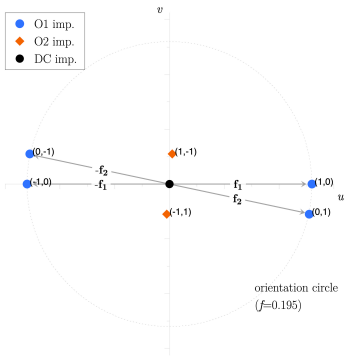

(c) Schematic representation of F

Figure 2: Two Ply Stack (2PS)

the textiles were not sheared during manipulation. An LLLW Prescale film was placed under the stack to record the pressure field exerted on the bottom plate. The two-layer stack was compressed over the pressure film by the imposed force. The pressure field retrieved after the compression is shown in Fig.2a. From a visual inspection of the image, one can notice the presence of bands in the pressure field, crossing from left to right with a rather uniform period. According to Moiré theory these bands are known as *Moiré fringes*. The patterns are analysed using spectral analysis. The grayscale pressure image is first inverted and its intensity normalized. Black lateral margins are added as needed to make the image square for performance optimization. No additional filtering is performed on the image. The two-dimensional Fast Fourier Transform (FFT) of the image is generated numerically and the spectrum is shifted to

Table 2: Two Ply Stack (2PS): impulses in the spectrum (Fig.2b)

Index	Order	Position (u, v)	Position (f, θ)	Amplitude	Source
$(0, 0)$	-	(0,0)	(0, 0°)	1	DC
$(1, 0)$	$\mathcal{O}1$	(52,0)	(0.1952, 0°)	0.45	layer 1
$(0, 1)$	$\mathcal{O}1$	(51,-11)	(0.1958, 12.16°)	0.37	layer 2
$(1, -1)$	$\mathcal{O}2$	(1,11)	$(0.0415, -84.8°)$	0.22	low Moiré
$(1, 1)$	$\mathcal{O}2$	(103,-11)	$(0.3888, 6.09°)$	0.16	high Moiré

center the zero-frequency impulse (DC). The resulting spectrum F in frequency domain u, v is plotted in Fig.2b, where only the magnification of the central region is shown. The spectrum is populated by precisely located pairs of twin impulses, in symmetric position from the origin and with complex conjugate amplitudes. In the remainder of this work, the amplitude values of impulses are to be intended as the magnitude of the complex amplitudes. The amplitude values are also normalized, which always results in the amplitude of the DC impulse being unity. For the purpose of analysis, a graphical scheme of the same region collecting the main impulses and their indexes is also provided on the side in Fig.2c. To interpret the physical meaning of each impulse we will adopt the classical index notation used in Moiré spectral analysis, which is detailed in Appendix A. The impulses present in the spectrum are listed in Table 2. The Cartesian u, v coordinates of impulses in the spectrum are expressed as pixel positions in the shifted frequency domain with the origin in the center. Polar coordinates f, θ are expressed in mm^{-1} and degrees respectively (clockwise rotation is positive). Twin impulses are omitted from the list. We can classify impulses under two groups: *first order* ($\mathcal{O}1$) and *second order* ($\mathcal{O}2$) impulses. $\mathcal{O}1$ impulses directly represent in frequency and orientation the generating cosinusoidal gratings that approximate the textile layers. Measuring the polar components (f, θ) of these impulses provides sufficient information to determine precisely the average orientation and spacing of the tow center-lines from the corresponding layer:

- the twin impulses (1,0) and (-1,0) identify a cosinusoidal grating oriented at $\theta_{1,0} = 0^\circ$ and of period $T_{1,0} = f_{1,0}^{-1} = 0.1952^{-1}\text{mm} = 5.12$ mm. This grating corresponds to the morphology of the first layer that was placed as the reference orientation $\theta = 0^\circ$ and had a period of $T_{\text{meas}} = 5.12$ mm.
- the impulses (0,1) and (0,-1) identify a cosinusoidal grating oriented at $\theta_{0,1} = 12.16^\circ$ and of period $T_{0,1} = f_{0,1}^{-1} = 0.1958^{-1}\text{mm} = 5.10$ mm. This grating corresponds to the second layer, which differs from the first only in orientation.

All the remaining impulses in the spectrum belong to the group of $\mathcal{O}2$ impulses. These originate from the convolution of $\mathcal{O}1$ impulses [22]. They are responsible for the band structures that one can perceive in the pressure field, i.e. the actual *Moiré fringes* that arise from the interference between layers.

- the twin impulses (1,-1) and (-1,1) identify some low frequency fringes (low Moiré) that run in the direction transverse to the tows. These bands are well within the circle of visibility [20] and are visually evident in Fig.2a.
- the impulses (1,1) and (-1,-1) define some higher frequency interference (high Moiré) between the layer gratings. They contribute to some extent to the definition of the pressure field, but at the same time their effect is less evident as one's sensitivity to high frequency detail decreases significantly [20].

To visually showcase their physical meaning, the individual pairs of $\mathcal{O}1$ and $\mathcal{O}2$ impulses present in the spectrum F have been isolated in Fig 3, where the corresponding cosinusoidal gratings from Eq.1 are plotted.

3.1.1. Validation

The validity of the spectrum analysis is compared to the direct visual measurement of the layer orientations. A picture of each layer being laid down is taken using a digital camera mounted in a fixed position from above. Layer orientations are measured

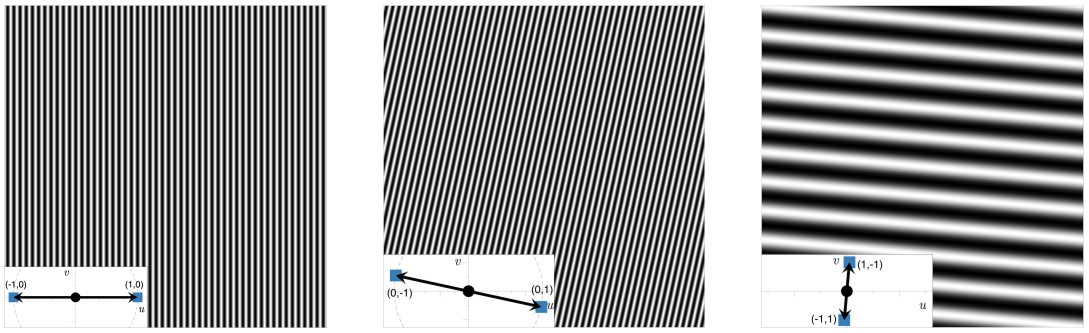

(a) $\mathcal{O}1$ impulse (1,0) - layer 1 (b) $\mathcal{O}1$ impulse (0,1) - layer 2 (c) $\mathcal{O}2$ impulse (1,-1) - low Moiré

Figure 3: Two Ply Stack (2PS): isolated impulses and associated gratings

manually using the software ImageJ [23]. Angle values are offset so that the bottom layer is the reference $\theta_1^{\text{vis}} = 0°$. The orientation of the second layer measured manually was $\theta_2^{\text{vis}} = 11.9°$, against the value measured in section 3.1 of $\theta_{0,1}^{\text{FFT}} = 12.16°$. The value measured from the pictures shows very good agreement with the one computed from the analysis of the pressure field spectrum. This proves that the physical interpretation of the impulses is satisfactory. However the values measured from the pictures hardly represent a benchmark for error estimation: in fact, it is reasonable to say that the uncertainty in the measurement of angles from the pictures (lens distortion, manual measurement precision) exceeds the uncertainty of measurement from analysing the position of an impulse. High sensitivity to small angle differences is a characteristic of Moiré analysis [18]. Therefore the visual validation is intended to be a confirmation of the physical interpretation of the spectrum rather than an error quantification.

3.1.2. Discussion on Two Ply Stack case

Some observations regarding this case can be elaborated. The first observation concerns $\mathcal{O}1$ impulses. Since the layers in the stack are made of the same textile, all $\mathcal{O}1$ impulses have a very similar frequency component ($f_{1,0} \approx f_{0,1}$) and only differ in orientation θ. In this case one can define a theoretical *orientation circle*, centered in the origin and with radius equal to the textile spatial frequency ($f_{1,0}$), on which all

$\mathcal{O}1$ impulses fall, their position depending only on their orientation. As a consequence, any $\mathcal{O}1$ impulse not located on the orientation circle becomes an indication of some uncontrolled distortion in the tows center-lines spacing of the corresponding layer that might have occurred during the compaction phase. The orientation circle then becomes a tool for the detection of deviations from the baseline configuration.

The second observation concerns $\mathcal{O}2$ impulses. According to the convolution theorem [22], the presence of $\mathcal{O}2$ impulses suggests that the pressure field exhibits characteristics of *multiplicative* interference rather than *additive*. An ideal additive field would not generate second-order impulses. (Moiré fringes could still be visible, but would rather be called *pseudo-Moiré* [24]). However the pressure field captured by the Prescale sensor is not a mathematical construct, but rather the result of a physical interaction between materials. Under the assumption of purely multiplicative interference of identical cosinusoidal gratings, such as Eq.A.2, all $\mathcal{O}1$ impulses in the FFT would have the same amplitude. This is not the case, as the amplitudes of $\mathcal{O}1$ impulses measured in Fig.2b are generally lower the farther away we move from the pressure sensor. This likely happens because the contact interaction between plies is non-linear, and affected by local variability of the material. Therefore it would be more appropriate to name this interference behavior *pseudo-multiplicative*. On the other hand, the sequential decrease in amplitude of $\mathcal{O}1$ impulses is useful because it reveals the ordering of plies in the stack.

3.2. Four Ply Stack

In real industrial applications fabric preforms are constructed with varying number of plies to build up to the thickness of the composite. In this section the method is extended to a Four Ply Stack (4PS) case. 4 layers of textile are stacked: the first ply is placed at a reference orientation (0°), then all subsequent layers are placed at some arbitrary, not pre-determined angles with respect to the reference layer (4 unique

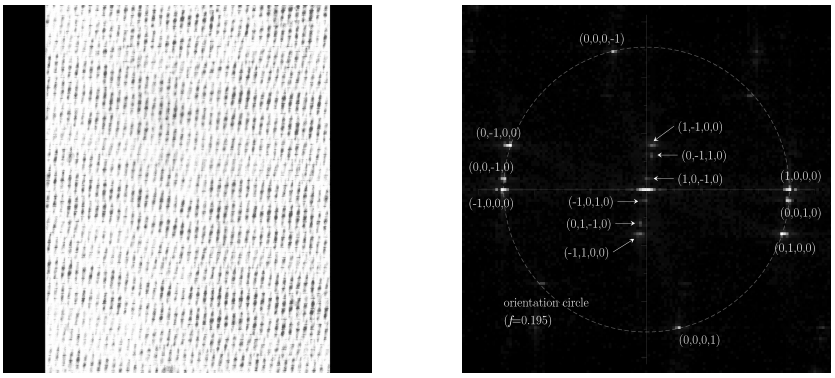

(a) Pressure field at 30 kN force (b) $F(u, v)$ spectrum data (enhanced contrast)

Figure 4: Four Ply Stack (4PS)

orientations are present in the stack). The same methodology of Section 3.1 is repeated. Pressure field and spectrum are shown in Fig.4, impulses are listed in Table 3. The interpretation remains unchanged: $\mathcal{O}1$ impulses describe the orientation and spatial frequency of the base layers. It can be observed that as the number of layers increases, impulses of higher order are also present in the spectrum ($\mathcal{O}2, \mathcal{O}3$, ... up to $\mathcal{O}N$ for N plies). They arise from the convolution of lower order impulses, hence their amplitude is lower, their contribution to the pressure field is negligible and will not be considered any further. In the 4PS case, orientations and spatial frequencies for all individual layers were measurable. Values were coherent with visual measurements of the same, which yielded the values, in the order: $0°, 18.5°, 4.2°, 76.5°$. It can be concluded that the spectral analysis of the pressure field allows one to fully detect the structure of multi-layer layups, up to at least 4 distinct orientations.

Discussion on Four Ply Stack case

It is well known that when gratings are at nearly orthogonal orientations the sensitivity of Moiré analysis is at its lowest [19]. The Four Ply Stack case shows that the technique is viable even when the angles are close to 90°. As already observed in the 2PS case, there is a progressive decrease in amplitude for all impulses when more

Table 3: Four Ply Stack (4PS): impulses in the spectrum (Fig.4b)

Index	Order	Position (u, v)	Position (f, θ)	Amplitude	Source
$(0, 0, 0, 0)$	-	(0,0)	(0, 0°)	1	DC
$(1, 0, 0, 0)$	$\mathcal{O}1$	(52,0)	(0.1956, 0°)	0.37	layer 1
$(0, 1, 0, 0)$	$\mathcal{O}1$	(49,-16)	(0.1940, 18.08°)	0.36	layer 2
$(0, 0, 1, 0)$	$\mathcal{O}1$	(51,-4)	(0.1948, 4.48°)	0.22	layer 3
$(0, 0, 0, 1)$	$\mathcal{O}1$	(12,-50)	(0.1945, 76.50°)	0.19	layer 4
$(1, 0, -1, 0)$	$\mathcal{O}2$	(0,4)	(0.0150, −90°)	0.10	low Moiré
$(0, -1, 1, 0)$	$\mathcal{O}2$	(2,12)	(0.0458, −80.53°)	0.10	low Moiré
$(1, -1, 0, 0)$	$\mathcal{O}2$	(2,16)	(0.0607, −82.87°)	0.11	low Moiré
$(1, 0, 0, -1)$	$\mathcal{O}2$	(40,50)	(0.2409, −51.34°)	0.06	low Moiré
$(0, 0, 1, -1)$	$\mathcal{O}2$	(39,46)	(0.2269, −49.71°)	0.04	low Moiré
$(0, 1, 0, -1)$	$\mathcal{O}2$	(37,34)	(0.1890, −42.58°)	0.08	low Moiré

orientations are introduced. Reasons behind the decay of $\mathcal{O}1$ impulses were discussed in section 3.1.2. On the other hand, the decrease in amplitude for all $\mathcal{O}1+$ impulses can indeed be explained by the convolution theorem: for every additional N^{th} layer a set of additional $\mathcal{O}N$ impulses are generated the amplitude of which decays with increasing order N as it is the product of the amplitudes of all $\mathcal{O}N-$ impulses that contribute in the convolution. This trend is qualitatively confirmed by the amplitude of all $\mathcal{O}1+$ impulses in the 4PS case. This property of the convolution theorem could be interpreted as unfavorable. However there is a way to turn this same property into an useful feature when addressing multi-layer layups, and this is detailed in the next section.

3.3. An application case study: misalignment detection in periodic layups

We propose here an example of scenario where one property of the convolution theorem is exploited to the benefit of the technique. In the layup of LCM preforms it is common practice to follow stacking sequences which are periodically repeated, for example: $[0°, 45°, 0°, 45°]$ or $[0°, 30°, 60°, 0°, 30°, 60°]$ and so on. The precise placement of each ply according to the designated orientation plays a major role in the final proper-

ties of the preform such as the local permeability and fiber volume fraction. While tools exist to assist the precise placement of every layer, a certain degree of misalignment from the prescribed values can occur. This is especially true in complex shape molds, where the distortion of the textiles being laid down can hinder the precise alignment. Obtaining a precise quantification of the deviation from the theoretical layup is not an easy task, especially when the misalignment originates during the compaction of the plies inside a closed mold. The methodology presented in this article can be applied to this scenario to evaluate the alignment between plies. To demonstrate this, the compaction of a Four Ply Periodic (4PP) layup, containing 4 plies in sequence $[0°, \theta_2, 0°, \theta_2]$, was repeated twice under different conditions. In the first scenario (4PPm) the stacking was performed allowing some slight misalignment between the layers pairwise in the sequence. In the second scenario (4PPa) great care was observed in aligning the layers two by two as precisely as possible. To keep the study as generic as possible, the angle θ for layers 2 and 4 was not pre-determined. This means that layer 2 was arbitrarily placed over layer 1, then layer 4 was placed to match precisely the orientation of layer 2.

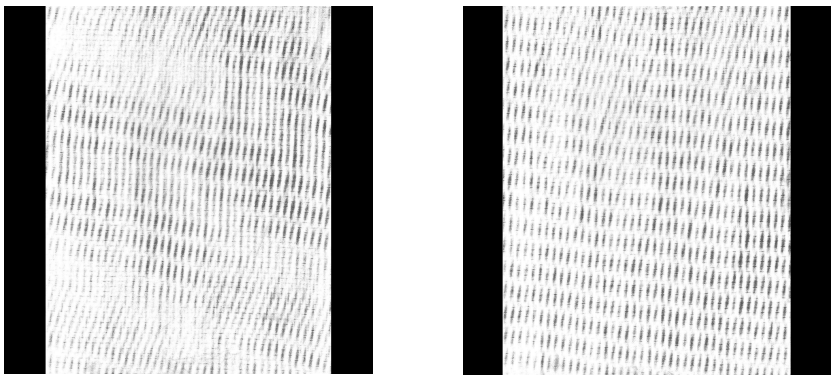

(a) 4PPm: slightly misaligned layers (b) 4PPa: well aligned layers

Figure 5: Four Ply Periodic (4PP): pressure field at 30 kN force

Table 4: 4PPm: impulses in the spectrum (Fig.6a)

Index	Order	Position (u, v)	Position (f, θ)	Amplitude	Source
$(0, 0, 0)$	DC	(0,0)	$(0, 0°)$	1	DC
$(1, 0, 0)$	$\mathcal{O}1$	(50÷52,0÷1)	$(0.1934, 0°)$	0.22	layers 1,3
$(0, 1, 0)$	$\mathcal{O}1$	(49,-14)	$(0.1913, 15.94°)$	0.28	layer 2
$(0, 0, 1)$	$\mathcal{O}1$	(48,-17)	$(0.1914, 19.50°)$	0.27	layer 4
$(1, -1, 0)$	$\mathcal{O}2$	(2,13)	$(0.0494, -81.25°)$	0.1	low Moiré
$(1, 0, -1)$	$\mathcal{O}2$	(3,16)	$(0.0611, -79.38°)$	0.12	low Moiré
$(0, 1, -1)$	$\mathcal{O}2$	(1,-3)	$(0.0119, -18.43°)$	0.12	low Moiré

Table 5: 4PPa: impulses in the spectrum (Fig.6b)

Index	Order	Position (u, v)	Position (f, θ)	Amplitude	Source
$(0, 0)$	-	(0,0)	(0,0°)	1	DC
$(1, 0)$	$\mathcal{O}1$	(51,0)	(0.1919,0°)	0.51	layers 1,3
$(0, 1)$	$\mathcal{O}1$	(48,-16)	(0.1941,18.43°)	0.49	layers 2,4
$(1, -1)$	$\mathcal{O}2$	(3,-16)	(0.0624,−79.37°)	0.29	low Moiré

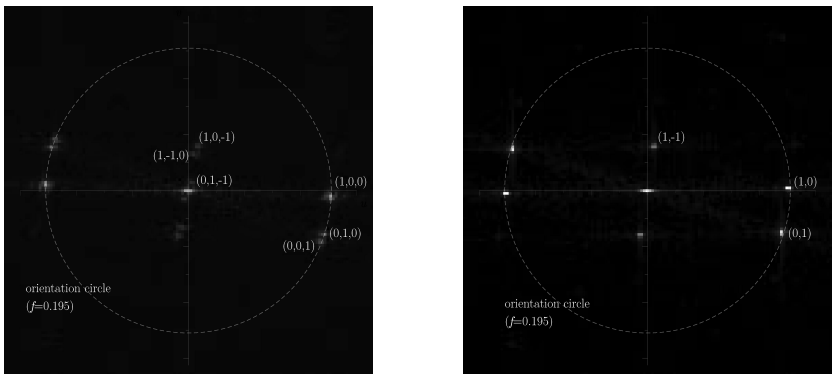

(a) 4PPm: slightly misaligned layers (b) 4PPa: well aligned layers

Figure 6: Four Ply Periodic (4PP): $F(u, v)$ spectrum data (enhanced contrast)

In test case 4PPm, the slightly misaligned layers generate the fairly structured pressure field shown in Fig.5a. One can notice visually the presence of two distinct low-frequency Moiré fringes on the image. After computing the FFT, shown in Fig.6a, it is possible to detect three distinct pairs of $\mathcal{O}1$ impulses that fall on the orientation circle. That is due to the fact that layers 2 and 4 are misaligned and are individually

detectable as separate impulses. Furthermore the (1,0,0) impulse appears blurry and its position is not well defined but spans several pixels. Values and detected orientations are provided in Table 4. On the other hand in test case 4PPa, when the plies are pairwise aligned with precision, only one set of Moiré fringes is present in the pressure field in Fig.5b. The spectrum in Fig.6b appears similar to the Two Ply Stack case addressed in section 3.1. Only two $\mathcal{O}1$ impulses are detectable: (1,0) and (0,1) mark the position of layers 1,3 and 2,4 respectively. Only two pairs of $\mathcal{O}2$ impulses are detected. Their amplitudes are higher than in test case 4PPm. Period and orientation of all layers can be accurately determined. Values are provided in Table 5. The multi-layer periodic layup scenario allows one to take advantage of a property of the convolution theorem: under the assumption of pseudo-multiplicative interference, the amplitudes of two impulses are summed when the convolution of the spectra places them in the same position in the frequency domain. This applies to impulses of all orders. This condition is met only when two layers are well aligned (they behave as one single layer), as in test case 4PPa, but not in test case 4PPm. An important consequence is that all *impulses in the misaligned scenario exhibit a lower amplitude than in the well-aligned scenario*, with $\mathcal{O}2$ impulses decaying faster that $\mathcal{O}1$. To confirm this finding, the same test was repeated for a Nine Ply Periodic (9PP) test case, with 9 layers stacked in periodic sequence $[0°, \theta_2, \theta_3, 0°, \theta_2, \theta_3, 0°, \theta_2, \theta_3]$. In test case 9PPm the layers were aligned roughly, while in test case 9PPa the layup was realised with extreme care, in order to effectively have only 3 unique orientations. Pressure fields for these two scenarios are shown in Figs. 7a, 7b. The corresponding FFT spectra are shown in Figs. 8a, 8b. In the spectrum of test case 9PPm a total of 5 $\mathcal{O}1$ blurry impulses can be detected, suggesting that at least 5 different orientations are present in the stack. On the other hand in the spectrum of test case 9PPa only 3 $\mathcal{O}1$ impulses can be detected, corresponding to the orientations $[0, \theta_1, \theta_2]$. Their position is well defined and their amplitude is higher than

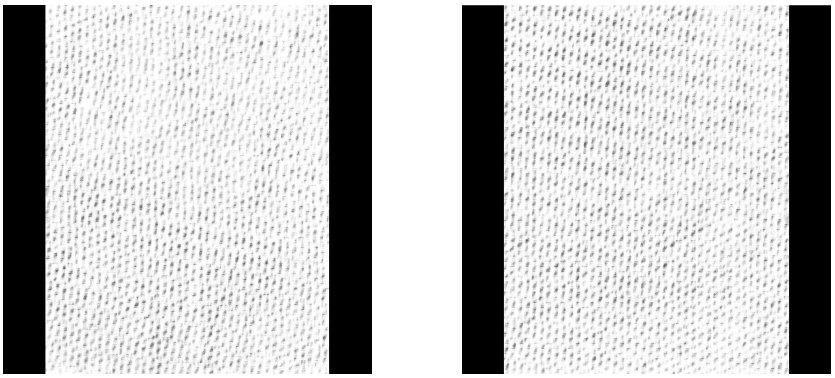

(a) 9PPm: slightly misaligned layers (b) 9PPa: well aligned layers

Figure 7: Nine Ply Periodic (9PP): pressure field at 30 kN

Table 6: 9PPm: impulses in the spectrum (Fig.8a)

Index	Order	Position (u, v)	Position (f, θ)	Amplitude	Source
(0,0,0,0,0)	-	(0,0)	(0,0°)	1	DC
(1,0,0,0,0)	$\mathcal{O}1$	(51,1)	(0.1919,−1.12°)	0.40	layers 1,4,7
(0,1,0,0,0)	$\mathcal{O}1$	(48,-17)	(0.1915,19.50°)	0.33	layers 2,5
(0,0,1,0,0)	$\mathcal{O}1$	(21,-47)	(0.1936,65.92°)	0.27	layers 3,9
(0,0,0,1,0)	$\mathcal{O}1$	(47,-21)	(0.1936,24.07°)	0.08	layer 8
(0,0,0,0,1)	$\mathcal{O}1$	(16,-49)	(0.1939,71.91°)	0.07	layer 6
(1,0,-1,0,0)	$\mathcal{O}2$	(30,48)	(0.2129,−58.00°)	0.13	low Moiré
(0,1,-1,0,0)	$\mathcal{O}2$	(27,29)	(0.1490,−47.04°)	0.12	low Moiré
(1,0,0,-1,0)	$\mathcal{O}2$	(3,18)	(0.0686,−80.53°)	0.08	low Moiré
(1,-1,0,0,0)	$\mathcal{O}2$	(5,23)	(0.0885,−77.73°)	0.04	low Moiré

the $\mathcal{O}1$ impulses from test case 9PPm. The periodic layup test cases 4PP and 9PP demonstrate that the analysis of the pressure field can provide information about orientations and spatial frequency of textile layers even in presence of a high number of plies. The results lead to two important conclusions:

- it is not the number of layers, but rather the number of *unique orientations* that defines the limit of the technique.

- for a given periodic layup, it is possible to assess the misalignment of layers by looking at the number and amplitude of the impulses present in the FFT of the pressure field. For example, a threshold value could be set on the amplitude of

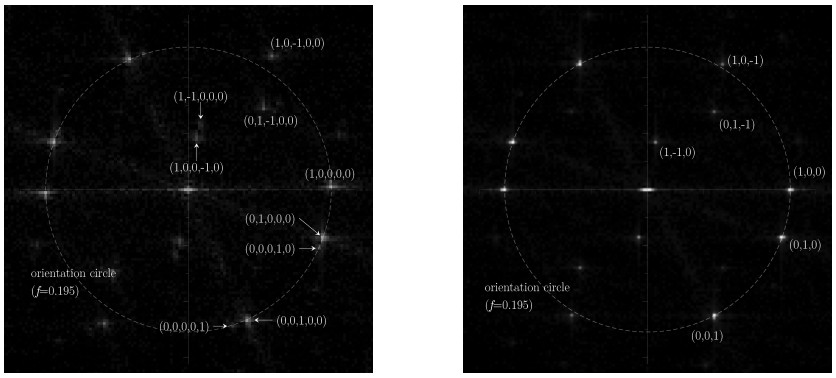

(a) 9PPm: slightly misaligned layers

(b) 9PPa: well aligned layers

Figure 8: Nine Ply Periodic (9PP): $F(u, v)$ spectrum data (enhanced contrast)

Table 7: 9PPa: impulses in the spectrum (Fig.8b)

Index	Order	Position (u, v)	Position (f, θ)	Amplitude	Source
$(0, 0, 0)$	-	(0,0)	(0,0°)	1	DC
$(1, 0, 0)$	$\mathcal{O}1$	(51,0)	(0.1919,0°)	0.44	layers 1,4,7
$(0, 1, 0)$	$\mathcal{O}1$	(48,-17)	(0.1916,19.50°)	0.35	layers 2,5,8
$(0, 0, 1)$	$\mathcal{O}1$	(24,-45)	(0.1919,61.92°)	0.29	layers 3,6,9
$(1, -1, 0)$	$\mathcal{O}2$	(3,17)	(0.0649,−80.00°)	0.18	low Moiré
$(1, 0, -1)$	$\mathcal{O}2$	(27,45)	(0.1974,−59.03°)	0.16	low Moiré
$(0, 1, -1)$	$\mathcal{O}2$	(24,28)	(0.1387,−49.40°)	0.15	low Moiré

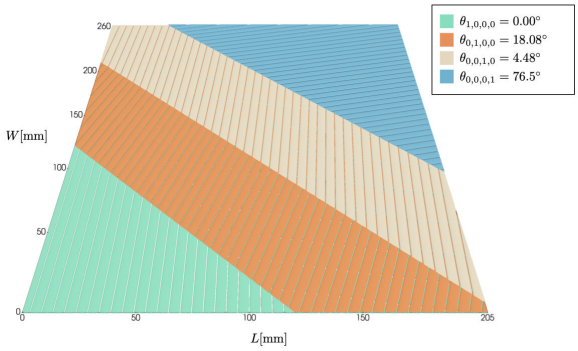

Figure 9: Digital reconstruction of the Four Ply Stack preform

$\mathcal{O}2$ impulses (which decay faster than $\mathcal{O}1$ in case of misalignment) to assess if the layup is acceptable or not.

3.4. Digital preform reconstruction

The generation of a digital textile is an example of how the Moiré analysis information can be exploited. There are several numerical tools available to generate a textile model: TexGen [25] and Wisetex [26] to name a few. In Fig. 9 we show an example created using TexGen: the values of orientation and center-line spacing from the Four Ply Stack case (Section 3.2) were used. Tow cross-sectional geometry is approximated by an ellipse. Tow width is set to the quantity measured in section 3.1 ($w = 4.80$mm), and tow thickness is obtained by dividing the final thickness h_f (Table 1) by the number of layers. For this test case, $h = h_f/4 = 2.67/4 = 0.67$mm).

One can see that the tow orientations and distribution are very accurately matching the ones measured from the real material, while on the other hand the tow cross sectional shapes are only approximated. An additional step would be to refine the geometry of tow cross sections. To this extent, mechanical models exist that compute the evolution of tow cross sections under compression [27, 28, 29, 10]. Their implementation however deserves a completely separate treatment and will not be dealt with in the present work. The numerical mesh of a multi-layer layup such as the one in Fig. 9 is the

typical domain input for further computations, such as mechanical or flow properties characterization of the fabric preform.

4. Conclusions

In this work we presented a new methodology to measure the layer orientations and tows spatial distribution of a multi-layer preform based on the analysis of its compaction pressure field. Measurements were obtained by combining the theory of Moiré interference with spectral analysis of images. For the first time it has been shown that this theory can be adopted for composite material application by exploiting the morphological similarity between periodic gratings and textile fabrics. The requirement for application of Moir é theory is that the layers present some degree of periodic waviness, which is always the case with textiles as they are composed by arrays of tows. The theory of Moiré notoriously ensures high precision in the detection of angles between layers when the misalignment is small. However we have demonstrated that, even in presence of high angles, the method yields accurate spatial description.

The main limiting factor encountered in the study is the maximum number of independent orientations that can be detected in the pressure field. For the textile in use, it was found to be 4. It is entirely possible that this value might increase or decrease if different materials or compaction forces are used. Still, it is not common to encounter real production preforms containing more than 4 independent orientations in the stack. The same reasoning applies to independent frequencies.

The potential of the methodology presented to the benefit of LCM processes is two-fold. First and foremost, it can detect the precise layer orientations and spatial frequency of tows in multi-layer preforms in their compacted state, which can be integrated with a description of the tows cross-sectional geometry to generate digital counterparts of the real material. Secondly, it can quantify the amount of misalign-

ment between supposedly aligned plies which is reflected directly in the amplitude and number of the impulses in the frequency domain. Unlike direct techniques such as μ-CT, the data acquisition is carried out by placing a Prescale pressure-sensitive film in the mold before compaction. One key aspect of this solution is the absence of measurement size limitations. Furthermore, the measurement is non-destructive, meaning that this technique could be integrated in current LCM manufacturing workflow to provide characterization of the dry preform before the filling is carried out. The main limit of the Prescale sensor is its poor capability of being sheared, which hinders its applicability to double-curvature moulds. However, this limitation could be worked around by performing a patchwork of films in reasonably flat locations, and inferring the properties in- between. More reasonably, the Prescale sensor is to be intended as a working solution, to be replaced by more flexible sensors in the view of an industrial application.

In the development of this novel method, quasi-UD textiles were used for their ease of interpretation and because they are often used in structural composites. Moiré theory however is able to interpret also interaction of periodic grids, and contributions exist in literature that apply the theory to non-periodic structures as well [30]. It is the authors' belief that the present methodology could be extended to woven fabric preforms and detection of tow path distortions.

Acknowledgements

This research was partially funded by Conseil Regional Pays de la Loire (grant number TEU29). The authors wish to thank A. C. Quintanilha for the precious help with the experimental work.

References

[1] S. G. Advani, E. M. Sozer, Process modeling in composites manufacturing, Vol. 59, CRC Press, 2002.

[2] M. V. Bruschke, S. G. Advani, A finite element/control volume approach to mold filling in anisotropic porous media, Polymer Composites 11 (6) (1990) 398–405. doi:10.1002/pc.750110613.

[3] S. Advani, K.-T. Hsiao, Handbook of Porous Media, Marcel Dekker, Inc., Madison Ave., NY, NY 10016, 2000, Ch. 19, pp. 845–891.

[4] K. M. Pillai, Modeling the unsaturated flow in liquid composite molding processes: A review and some thoughts, Journal of Composite Materials 38 (23) (2004) 2097–2118. doi:10.1177/0021998304045585.

[5] M. Akbari, M. Bahrami, D. Sinton, Analytical and experimental characterization of flow in slowly-varying cross-section microchannels, American Society of Mechanical Engineers, Fluids Engineering Division (Publication) FEDSM 1 (PARTS A, B AND C) (2010) 2161–2170. doi:10.1115/FEDSM-ICNMM2010-30417.

[6] X. Zeng, A. Endruweit, L. P. Brown, A. C. Long, Numerical prediction of in-plane permeability for multilayer woven fabrics with manufacture-induced deformation, Composites Part A: Applied Science and Manufacturing 77 (2015) 266–274. doi:10.1016/j.compositesa.2015.03.027.
URL `http://dx.doi.org/10.1016/j.compositesa.2015.03.027`

[7] A. Endruweit, A. C. Long, F. Robitaille, C. D. Rudd, Influence of stochastic fibre angle variations on the permeability of bi-directional textile fabrics, Composites Part A: Applied Science and Manufacturing 37 (1) (2006) 122–132. doi:10.1016/j.compositesa.2005.04.014.

[8] E. E. Swery, T. Allen, P. Kelly, Automated tool to determine geometric measurements of woven textiles using digital image analysis techniques, Textile Research Journal 86 (6) (2016) 618–635.

[9] F. Gommer, L. P. Brown, R. Brooks, Quantification of mesoscale variability and geometrical reconstruction of a textile, Journal of Composite Materials 50 (23) (2016) 3255–3266.

[10] S. Bancora, C. Binetruy, S. Advani, S. Comas-Cardona, Inverse methodology as applied to reconstruct local textile features from measured pressure field, Journal of Materials Science & Technology 71 (2021) 241–247.

[11] F. Desplentere, S. V. Lomov, D. Woerdeman, I. Verpoest, M. Wevers, A. Bogdanovich, Micro-ct characterization of variability in 3d textile architecture, Composites Science and Technology 65 (13) (2005) 1920–1930.

[12] A. Liggins, The practical application of fuji prescale pressure-sensitive film, in: Optical measurement methods in biomechanics, Springer, 1997, pp. 173–189.

[13] B. Chen, E. J. Lang, T.-W. Chou, Experimental and theoretical studies of fabric compaction behavior in resin transfer molding, Materials Science and Engineering: A 317 (1-2) (2001) 188–196.

[14] W. Walbran, S. Bickerton, P. Kelly, Measurements of normal stress distributions experienced by rigid liquid composite moulding tools, Composites Part A: Applied science and manufacturing 40 (8) (2009) 1119–1133.

[15] W. Chen, X. Yan, Progress in achieving high-performance piezoresistive and capacitive flexible pressure sensors: A review, Journal of Materials Science & Technology (2020).

[16] S. Lee, A. Reuveny, J. Reeder, S. Lee, H. Jin, Q. Liu, T. Yokota, T. Sekitani, T. Isoyama, Y. Abe, et al., A transparent bending-insensitive pressure sensor, Nature nanotechnology 11 (5) (2016) 472.

[17] A. Liggins, J. Stranart, J. Finlay, C. Rorabeck, E. Little, Calibration and manipulation of data from fuji pressure-sensitive film, Exp Mech 1992 (1992) 61–70.

[18] D. Post, B. Han, P. Ifju, High sensitivity moiré: experimental analysis for mechanics and materials, Springer Science & Business Media, 2012.

[19] I. Amidror, The Theory of the Moiré Phenomenon: Volume I: Periodic Layers, Vol. 38, Springer Science & Business Media, 2009.

[20] I. Amidror, R. D. Hersch, The role of fourier theory and of modulation in the prediction of visible moiré effects, Journal of Modern Optics 56 (9) (2009) 1103–1118.

[21] K. Patorski, K. Pokorski, M. Trusiak, Fourier domain interpretation of real and pseudo-moiré phenomena, Optics express 19 (27) (2011) 26065–26078.

[22] R. N. Bracewell, R. N. Bracewell, The Fourier transform and its applications, Vol. 31999, McGraw-Hill New York, 1986.

[23] C. A. Schneider, W. S. Rasband, K. W. Eliceiri, Nih image to imagej: 25 years of image analysis, Nature methods 9 (7) (2012) 671.

[24] I. Amidror, R. D. Hersch, The role of Fourier theory and of modulation in the prediction of visible moire effects, Journal of Modern Optics 56 (9) (2009) 1103–1118. doi:10.1080/09500340902994140.

[25] H. Lin, L. P. Brown, A. C. Long, Modelling and simulating textile structures using

texgen, in: Advanced Materials Research, Vol. 331, Trans Tech Publ, 2011, pp. 44–47.

[26] I. Verpoest, S. V. Lomov, Virtual textile composites software wisetex: Integration with micro-mechanical, permeability and structural analysis, Composites Science and Technology 65 (15-16) (2005) 2563–2574.

[27] E. Sozer, B. Chen, P. Graham, S. Bickerton, T. Chou, S. Advani, Characterization and prediction of compaction force and preform permeability of woven fabrics during the resin transfer molding process, in: FPCM-5: Fifth International Conference on Flow Processes in Composite Materials, 1999, pp. 25–35.

[28] S. A. Grishanov, S. V. Lomov, R. J. Harwood, T. Cassidy, C. Farrer, The simulation of the geometry of two-component yarns. Part I: The mechanics of strand compression: Simulating yarn cross-section shape, Journal of the Textile Institute 88 (2) (1997) 118–131. doi:10.1080/00405009708658536.

[29] A. S. Dharmalingam, J. Hemmer, A. S. Lectez, C. Binetruy, S. Comas-Cardona, Evolution of single carbon and glass fibrous tow cross-sections in dry and lubricated states during compaction perpendicular to the fibers, Composites Part B: Engineering 148 (March) (2018) 235–242. doi:10.1016/j.compositesb.2018.05.001. URL https://doi.org/10.1016/j.compositesb.2018.05.001

[30] I. Amidror, The Theory of the Moiré Phenomenon: Volume II: Aperiodic Layers, Vol. 34, Springer Science & Business Media, 2009.

[31] A. Rosenfeld, Digital picture processing, Academic press, 1976.

Appendix A. Spectral Moiré analysis

In this Appendix, which relies heavily on material from [19], a short summary of Moiré spectral analysis and notation is provided. Moiré artifacts can be observed when two or more periodic structures are superimposed. In the present study we focus on gratings-like structures, as they resemble closely the yarn arrays of textiles commonly found in composite layups. We define a raised cosinusoidal grating by the function:

$$g(x, y) = \frac{1}{2}\cos[2\pi f(x\cos\theta + y\sin\theta)] + \frac{1}{2} \tag{A.1}$$

where f represents the frequency per unit length and θ defines the normal orientation of the grating. This spatial function assumes values between 0 and 1, therefore can easily be represented as a grayscale image bounded by its extrema (0 is black, 1 is white). In Figs. A.10a,A.11a two such gratings g_1 and g_2 are represented, over a unit domain, with frequency $f = 20$ and orientations $\theta_1 = 0°$ and $\theta_2 = 20°$ respectively. Moiré effects arise when gratings are superimposed, which can be carried out in two ways: *multiplicative* superposition or *additive/subtractive* superposition. In this work we focus only on multiplicative superposition, which for two gratings g_1 and g_2 is expressed as:

$$G(x, y) = g_1(x, y) \cdot g_2(x, y) \tag{A.2}$$

The image $G(x, y)$ resulting from this operation is shown in Fig. A.12a. One can notice visually that a series of low frequency periodic bands arise from the interaction of the base arrays. We will refer to these bands as *moiré fringes*.

The best tool for investigation of this new structure is image spectral analysis. The 2D Fourier transform is performed numerically (FFT) on on $G(x, y)$ and the resulting spectrum is shifted to center the zero-frequency. The result is the spectrum F_G shown in Fig.A.12b, where the central portion of the image which contains the frequency

(a) $g_1(x, y)$ (b) $F_1(u, v)$

Figure A.10: The function g_1 and its spectrum F_1

information has been magnified for the sake of clarity. The spectrum contains a series of impulses, each characterized by a position vector and an amplitude. Each impulse is paired with an identical twin impulse which is symmetrical from the origin. The position vector of an impulse is expressed in polar coordinates by its distance f from the origin and the angle θ the vector makes with the u axis. These values match the frequency and orientation of the periodic grating g associated to that impulse. Every impulse is also characterized by an amplitude. Position and amplitude of each impulse are dictated by the convolution theorem [22] which states that the Fourier transform of the product of functions is the *convolution* of the Fourier transforms of the individual functions.

$$F_G(u, v) = [F_1 * F_2](u, v) \tag{A.3}$$

The convolution of the spectra F_1 and F_2 can be geometrically defined by placing over each of the impulses of F_1 a centered copy of F_2 or vice-versa [31]. As a consequence, we can identify two groups of impulses in F_G. First we can locate the impulses that correspond to the generating layers, that we will name *first order* ($\mathcal{O}1$) impulses. Their position is described by the corresponding frequency vectors:

- $\mathbf{f}_1$ at polar coordinates $(20, 0°)$: identifies the grating g_1, see Fig.A.10

(a) $g_2(x, y)$ (b) $F_2(u, v)$

Figure A.11: The function g_2 and its spectrum F_2

- $\mathbf{f}_2$ at polar coordinates $(20, 17°)$: identifies the grating g_2, see Fig.A.11

We can also locate two new pairs of impulses which frequencies were not present in the original gratings. As a consequence of the convolution theorem the location of these impulses is obtained as the sum and difference of the frequency vectors of the base impulses being convoluted. Their amplitude is the product of the amplitudes of the impulses participating in the convolution. We will name these *second order* ($\mathcal{O}2$) impulses:

- a set of low frequency impulses, at location $\mathbf{f}_1 - \mathbf{f}_2$ and $\mathbf{f}_2 - \mathbf{f}_1$

- a set of high frequency impulses, at location $\mathbf{f}_1 + \mathbf{f}_2$ and $-\mathbf{f}_1 - \mathbf{f}_2$

A convenient index notation exists that allows to identify every impulse by expressing it as a linear combination of all the n generating impulses, and collecting the integer coefficients in the form $(k_1, ..., k_n)$. In Table A.8 are listed all the impulses present in the spectrum F_G of G, as well as their geometric coordinates and their indices.

We define the $\mathcal{O}2$ impulse (1,-1) and its twin (-1,1) as *low Moiré* because they generate the low frequency structures known as *Moiré fringes* that are clearly visible on G. On the other hand, the $\mathcal{O}2$ impulse (1,1) and its twin (-1,-1) are *high Moiré* because they contribute to G with some high frequency patterns which are hardly

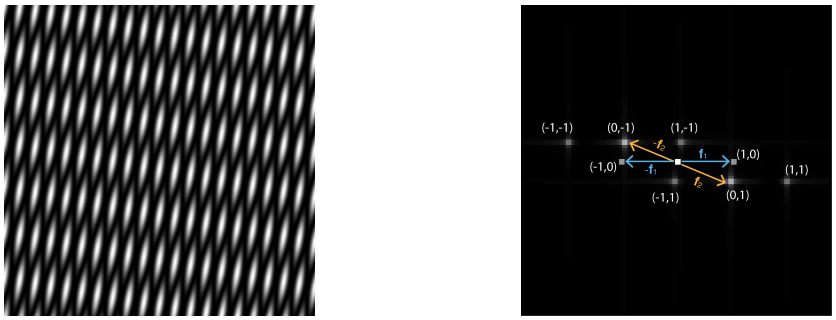

(a) $G(x, y)$ (b) $F_G(u, v)$

Figure A.12: The product function G and its spectrum F_G

Table A.8: Impulses collected from the spectrum F_G

Vector	Lin. comb.	Index	Order	Position (u, v)	Position (f, θ)	Amplitude	Source
$\mathbf{f}_0$	$0\mathbf{f}_1 + 0\mathbf{f}_2$	(0,0)	-	(0,0)	$(0, 0°)$	0.25	DC
$\mathbf{f}_1$	$1\mathbf{f}_1 + 0\mathbf{f}_2$	(1,0)	$\mathcal{O}1$	(20,0)	$(20, 0°)$	0.125	g_1
$-\mathbf{f}_1$	$-1\mathbf{f}_1 + 0\mathbf{f}_2$	(-1,0)	$\mathcal{O}1$	(-20,0)	$(20, -180°)$	0.125	g_1
$\mathbf{f}_2$	$0\mathbf{f}_1 + 1\mathbf{f}_2$	(0,1)	$\mathcal{O}1$	(19,-7)	$(20, 17°)$	0.125	g_2
$-\mathbf{f}_2$	$0\mathbf{f}_1 - 1\mathbf{f}_2$	(0,-1)	$\mathcal{O}1$	(-19,7)	$(20, -163°)$	0.125	g_2
$\mathbf{f}_1 - \mathbf{f}_2$	$1\mathbf{f}_1 - 1\mathbf{f}_2$	(1,-1)	$\mathcal{O}2$	(1,7)	$(7.07, -81.8°)$	0.0625	low Moiré
$-\mathbf{f}_1 + \mathbf{f}_2$	$-1\mathbf{f}_1 + 1\mathbf{f}_2$	(-1,1)	$\mathcal{O}2$	(-1,-7)	$(7.07, 98.2°)$	0.0625	low Moiré
$\mathbf{f}_1 + \mathbf{f}_2$	$1\mathbf{f}_1 + 1\mathbf{f}_2$	(1,1)	$\mathcal{O}2$	(39,-7)	$(39.6, 10°)$	0.0625	high Moiré
$-\mathbf{f}_1 - \mathbf{f}_2$	$-1\mathbf{f}_1 - 1\mathbf{f}_2$	(-1,-1)	$\mathcal{O}2$	(-39,7)	$(39.6, -170°)$	0.0625	high Moiré

distinguishable at visual observation [20]. Finally the central impulse, traditionally named DC, has a frequency value equal to 0, undefined θ and represents the average intensity of G.

Graphical Abstract

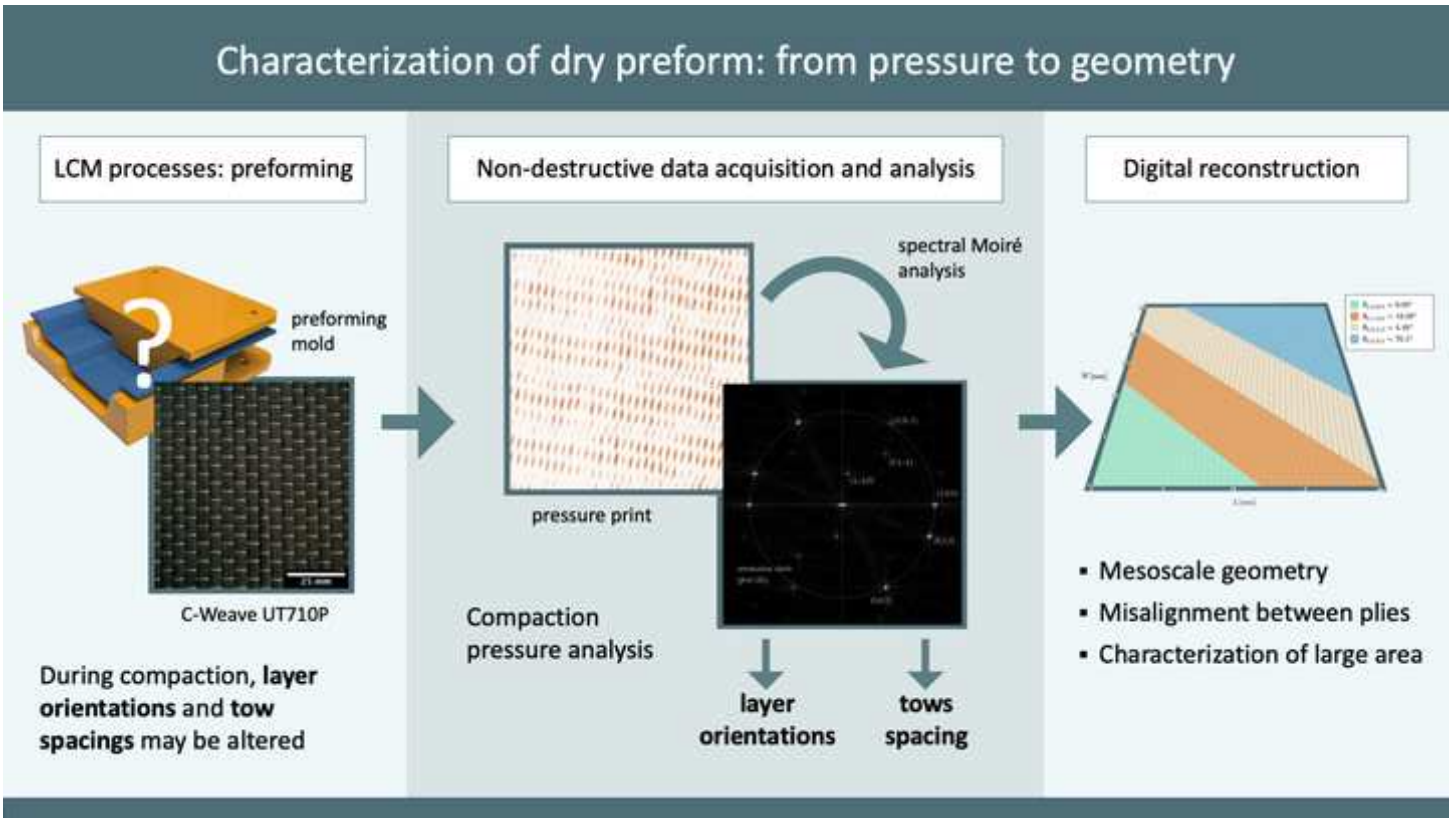

CREDIT AUTHOR STATEMENT

Simone Bancora: Conceptualization, Methodology, Investigation, Writing - Original draft preparation.
Christophe Binetruy: Supervision, Methodology, Writing - Reviewing and Editing
Suresh Advani: Supervision, Methodology, Writing - Reviewing and Editing
Sébastien Comas-Cardona: Supervision, Methodology, Writing - Reviewing and Editing

Declaration of interests

√ The authors declare that they have no known competing financial interests or personal relationships that could have appeared to influence the work reported in this paper.

☐The authors declare the following financial interests/personal relationships which may be considered as potential competing interests: